UAV imagery

Digital elevation models of underwater structures from UAV imagery

An article by CHRISTIAN MULSOW

The paper presents a workflow for the generation of digital elevation models (DEMs) of underwater areas from aerial images. Standard software products do not provide the possibility to triangulate correctly through refractive interfaces, such as water. Known procedures are based on oriented images and known water levels with DEM determination via forward intersection based on reconstructed image ray paths (ray tracing). In this article an integrated procedure for image orientation as well as DEM extraction from aerial imagery containing both land and underwater areas is presented. The proof of concept was done by capturing UAV imagery of shallow water areas of a high-alpine lake in the Swiss Alps. The processed data set will be presented and the extraction and matching of image points observed through water are discussed. The accuracy potential as well as practical limitations of processing multimedia data are analysed.

UAV | DEM | underwater | multimedia | bundle adjustment

Author

Christian Mulsow works at the Institute of Photogrammetry and Remote Sensing, TU Dresden.

christian.mulsow@tu-dresden.de

1   Motivation

The talus slope at Flüelapass was the first mountain permafrost study site in Switzerland in the Alps, and the presence of ice-rich permafrost at the foot of the slope has first been researched by Haeberli (1975). Recent investigations led to new hypotheses on the geomorphological processes at the study site (Kenner et. al 2017). One important data set for the research was a digital elevation model (DEM) of the area, which also includes the bottom of a lake named Schottensee (see Fig. 1). To survey such regions by photogrammetry, we have to account for the two different media, air and water.

2   UAV data set

The use of UAV imagery became standard for DEM generation of small areas in the last few years. They fill the gap between terrestrial laser scanning (TLS) as well as conventional aerial photogrammetry and airborne laser scanning (ALS). Therefore, a UAV image block was seen as suitable database for DEM generation for the study site.

In September 2016, a block of aerial images was acquired with a Sony NEX-7 camera (24 Mp, 20 mm, F/2.8 optical lens) mounted on an Ascending Technologies (AscTec) Falcon 8 octocopter (Bühler et al. 2016). About 300 images were taken from a flying height of 100 m above ground (GSD of 2 cm) with an overlap of approximately 75 % along track and 65 % across track. Initial camera positions and orientations were taken from UAV's GNSS- and IMU-system while heading was available only. Eight ground control points were signalised on land, whose coordinates were defined using a Topcon GR5 GNSS receiver in real time kinematic mode.

As Fig. 2 shows, the distribution of control points is far from ideal for a stable geo-referencing of the whole block. However, the region of interest, in that case the slope and the lobe area, is covered sufficiently. Due to the lack of suitable equipment and access, no underwater control points were installed. This limits a stable absolute orientation as well as a rigorous quality control (position and height) of images showing underwater areas mainly.

A few months after the UAV campaign, several underwater checkpoints were measured via GPS for quality control. A first set was measured through water in November 2016 and a second through ice in December 2016. Fig. 3 shows the positions of used checkpoints. Checkpoints could be measured in situ up to a water depth of 2.8 m.
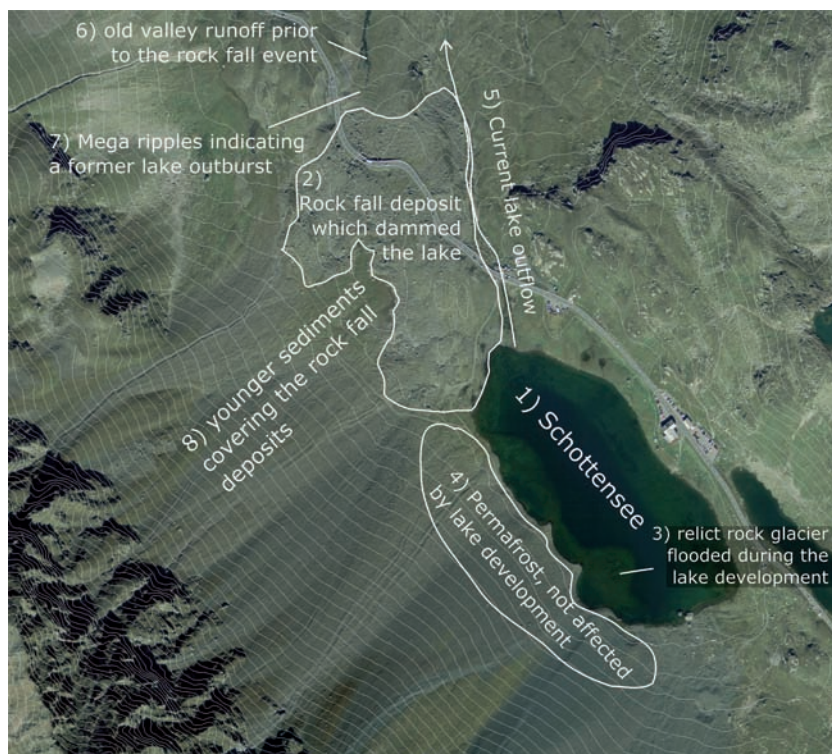

Fig. 1: Orthophoto of the Flüelapass. The labelled landforms give in their numbered order a short overview on the geomorphologic history of the site
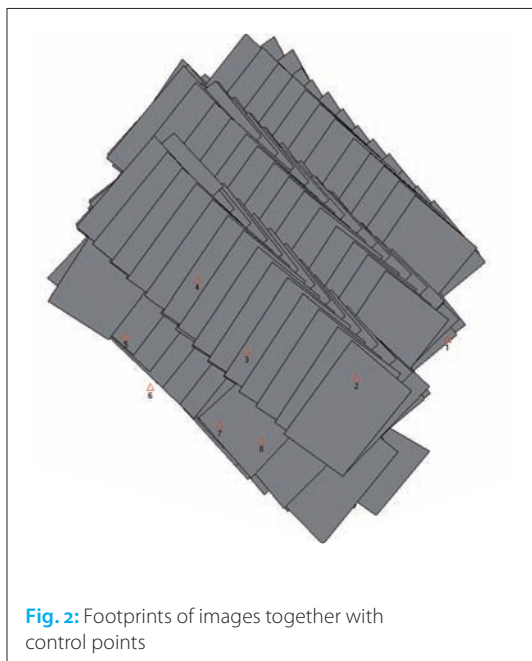
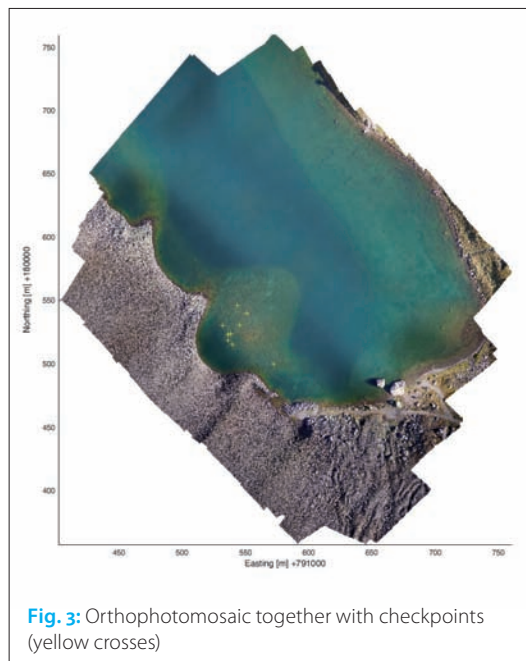**Fig. 2:** Footprints of images together with control points

Fig. 3: Orthophotomosaic together with checkpoints (yellow crosses)

3   Multimedia bundle adjustment

The refraction has to be taken into account when measuring through refracting surfaces. In contrast to the one-media case (usually air), the camera and the object of interest are not in the same optical media. Therefore, the ray between the perspective centre of the camera and an object point is not a straight line. The image ray changes direction while passing the interface between the different medias, following Snell's law. Consequently, the extension of standard photogrammetric imaging models is required.

In aerial photogrammetry, the two-media-problem (air and water) has been discussed since the 1940s. Rinner (1948) proposed the stepwise reduction of the problem down to known procedures of standard (one-media) photogrammetry on analogue instruments. First practical aspects of water depths measurements from aerial photographs were highlighted by Tewinkel (1963). Several compensation methods for refraction effects were published over the decades, like Fryer (1983) or Butler et. al. (2002). Generally, these methods just add a correction to derived underwater-point coordinates. Usually, the images had to be orientated separately and the water surface had to be known. First thoughts for an integrated bundle adjustment for multimedia imagery were published by Kotowski (1987). Maas (2015) presented a multimedia module for planar interfaces which can easily be integrated into photogrammetric standard tools such as spatial resection, spatial intersection or bundle adjustment.

An integrated bundle adjustment software was developed by Mulsow et.al. (2010) based on the work of Kotowski (1987). In Kotowski's universal model, the coordinates of the refraction point nearest to the camera (P_1 in Fig. 4) defines the image ray together with the projection center P_0 and the image point p' on the sensor.

The mathematical model is based on the well known collinearity equation. Here, the object point P is substituted with the refraction point nearest to the projection centre (P_1).

$$x' = x'_0 + z' \frac{r_{11}(X_1-X_0) + r_{21}(Y_1-X_0) + r_{31}(Z_1-X_0)}{r_{13}(X_1-X_0) + r_{23}(Y_1-X_0) + r_{33}(Z_1-X_0)} + \Delta x'$$

$$y' = y'_0 + z' \frac{r_{12}(X_1-X_0) + r_{22}(Y_1-X_0) + r_{32}(Z_1-X_0)}{r_{13}(X_1-X_0) + r_{23}(Y_1-X_0) + r_{33}(Z_1-X_0)} + \Delta y'$$

with:

X_1, Y_1, Z_1 : object points of refracting point P_1 nearest to the projection centre
$r_{11} - r_{33}$: elements of 3×3 rotation matrix R
x'_0, y'_0 : coordinates of the principal point
$\Delta x', \Delta y'$: axis related correction values for imaging errors (e.g. lens distortion)

The main task in this approach is the complete reconstruction of the image ray path through two or
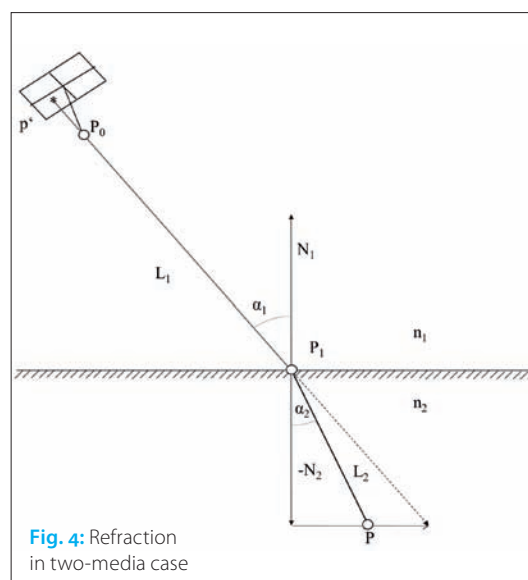

Fig. 4: Refraction in two-media case

more optical media with different refractive indices (ray tracing):

$$(X_{1ij}^I, Y_{1ij}^I, Z_{1ij}^I) = f_{P_1}(X_{0j}, Y_{0j}, Z_{0j}, X_i, Y_i, Z_i, a^I, n^I)$$

with:

i : point index
j : image index
I : set of indexes of interfaces t
a^I : set of parameters of interfaces a_t
n^I : set of refractive indices n_t
t : index of interface

The system of collinearity equations together with the ray tracing is non-linear. For solving, the least squares estimation in the Gauss-Markov model can be used. The necessary linearisation of the collinearity equations cannot be done analytically due to the (iterative) ray tracing. Instead, the differential quotients can be determined via numerical differentiation. The computational effort for differentiation can be large, due to the iterative ray tracing for each differential quotient and for each iteration of the solving algorithm for the collinearity equation.

The main advantages of this solution are its universality and flexibility as well as the possibility to implement it into conventional bundle adjustment. The implemented multimedia-bundle was applied to several tasks (Mulsow et. al. 2010; Mulsow et. al. 2014a), where the method could prove its main advantage: as in a conventional bundle-adjustment, all parameters (interior and exterior orientation, new-point coordinates) can be treated as unknowns. Additionally, the surface parameters of interfaces between different media, new-points in other media as well as refractive indices can be computed in one integrated adjustment. An in-

depth description of the mathematical model together with different ray tracing strategies can be found in Mulsow et. al. (2010) and Mulsow (2016).

4   Image orientation

In a first step, the number of images was reduced to a feasible level. Blurred images as well as overexposed and underexposed material were sorted out. Further, only images covering the region of interest (slope and lobe) were held in the block. Fig. 5 shows the block-layout for processing.

The whole block was first processed conventionally in LPS 9.3 (ERDAS, Hexagon) in order to obtain corresponding points and initial values for image orientations. Image points were measured automatically, which failed for some deeper areas due to low contrast. For this areas, some additional tie points were measured manually. In a second step, the underwater points were labelled manually.

A number of 41 images was processed, of which six images with water coverage of at least 70 %. About 8000 image measurements were handed over for further processing. Images were connected by ~900 tie points, of which ~150 were labelled as underwater points. In order to achieve best results, all manually measured image points were refined by least squares matching (LSM) in a self-written software.

In order to evaluate the best strategy for processing, several parameter settings were applied for bundle adjustment:

I. Adjustment based on all measured image points, all labelled as onshore points.

II. Adjustment based onshore points exclusively for camera calibration and image orientation of images with at least 70 % of onshore coverage.

III. Adjustment with fixed camera calibration parameters as well as already oriented onshore images (from II) plus remaining un-oriented images (>30 % water coverage), underwater points together with onshore points.

IV. Adjustment with maximum degree of freedom, all image data used, camera parameters as well as orientations were treated as unknowns, image points labelled as onshore points or underwater points.

The simultaneous estimation of water-surface parameters as well as refraction index of water failed due to high correlations between parameters caused by the near-vertical incidence angles of image rays (max angle ~20°) and the limited water depth to flight-height ratio.

The compiled results are listed in the table. When analysing the quality parameters of the processing versions, configuration III can be identified as best suited for given data based on the fit of the derived heights with underwater checkpoints speaks for that parametrisation strategy.

At first glance, the internal height-precision of the underwater points in object space is best for configuration I. Actually, this high accuracy is caused by the refraction effect which is still included in the cal-

References

Bühler, Yves; Marc S. Adams; Ruedi Bösch; Andreas Stoffel (2016): Mapping snow depth in alpine terrain with unmanned aerial systems (UASs): potential and limitations; The Cryosphere, Vol. 10, No. 3, pp.1075–1088, 10.5194/tc-10-1075-2016

Butler, Justin; Stuart Lane; Jim Chandler; Ekaterini Porfiri (2002): Through-Water Close Range Digital Photogrammetry in Flume and Field Environments; The Photogrammetric Record, Vol. 17, No. 99, pp. 419–439, DOI: 10.1111/0031-868X.00196

Fryer, John G. (1983): Photogrammetry through shallow water; Australian Journal of Geodesy, Photogrammetry and Surveying, Vol. 38, pp. 25–38

Fryer, John G.; C. S. Fraser (1986): On the calibration of underwater cameras; The Photogrammetric Record, Vol. 12, No. 67, pp. 73–85, DOI: 10.1111/j.1477-9730.1986.tb00539.x

Glassner, Andrew S. (1989): An Introduction to Ray Tracing; Academic Press, London

Haeberli, Wilfried, 1975. Untersuchungen zur Verbreitung von Permafrost zwischen Flüelapass und Piz Grialetsch (Graubünden); Mitteilungen der Versuchsanstalt für Wasserbau, Hydrologie und Glaziologie der ETH Zürich, Vol. 17, 221 pp.

…

Fig. 5: Reduced image block processed in multimedia-bundle

Quality parameter	Parameter setting no.			
	I	**II**	**III**	**IV**
S_o [px]	0.48	0.47	0.49	0.49
RMS x' y' land [px]	0.43/0.44	0.42/0.43	0.42/0.43	0.43/0.44
RMS x' y' water [px]	0.44/0.43	–	0.51/0.51	0.46/0.46
c_k [mm]	20.443	20.467	20.467	20.441
x_H [mm]	−0.0027	−0.0018	−0.0018	−0.0030
y_H [mm]	0.0584	0.0552	0.0522	0.0587
RMS X/Y/Z land [cm]	1.7/1.4/4.4	1.5/1.2/3.8	1.5/1.2/3.8	1.7/1.4/4.4
RMS X/Y/Z water [cm]	1.0/1.7/4.4	–	0.9/1.6/5.3	1.0/1.8/6.0
	Underwater checkpoints			
RMS Z [cm]	2.9	–	3.5	4.0
RMS $Z_{target} - Z_{actual}$ [cm]	65.8	–	11.8	14.5

culated point heights here. Not taking the refraction into account, leads to larger intersection angles for image rays of underwater points. When considering refraction, the image ray intersection angle in the denser medium (water) becomes smaller (Maas 2015), thus degrading the accuracy. As expected, the quality of image-point measurements of underwater points is lower than of onshore points. A degrading factor of 1.4 can be derived from triangulation results (parameter setting III).

5 Underwater DTM extraction

The workflow for underwater DTM extraction follows the way of processing conventional data sets. First, homological point pairs in stereo images has to be identified and measured. In a second step, the corresponding image rays are intersected in order to obtain the point coordinates. Finally, the point cloud can be transformed into a TIN (triangulated irregular network).

5.1 Image processing

In a first step, image pairs were defined and transformed into normal images in order to provide some kind of y-parallax-free stereo images for matching. From theory, the epipolar lines are not straight in multimedia case. However, due to the low water depth the epipolar lines can be seen as straight to a certain degree.

Similar to common matching-procedures, an image-pyramid strategy was implemented. Starting with lowest resolution (reducing-factor 5), points-of-interest were extracted. In order to achieve a good coverage, a raster (75×50 cells) was defined for the reference image and for each raster cell the best Harris-point was extracted. These points were searched and measured in the partner image via LSM (patch size 21×21, shift in x direction and one scale parameter only). From matched point pairs, a disparity map was computed. In the next pyramid step, again a raster was defined for the reference image and Harris-points were extracted. Thanks to the disparity map from the previous pyramid step, the search-space can be reduced significantly for matching. The iterative procedure is continued until

the finest resolution-level of the image-pyramid is reached. Finally, the matched point pairs are transferred to the original images and were matched again, but now with a full-parameter set for LSM.

5.2 Multimedia forward intersection

Based on the orientations and camera parameters from aerial triangulation configuration III, the image measurements can be projected into the object space. For each image point an image ray can be computed. An automated labelling land- and underwater points can be made based on calculated point heights. Therefore, all image point pairs are processed via conventional forward intersection first. By thresholding the calculated heights by the known water level (from GPS measurements), points below the water level can be labelled as underwater points, and points above as land points. Image point pairs labelled as underwater point are to be processed via multimedia forward intersection procedure.

In a first step, the image ray is projected into the object space, as mentioned before. In a second step, the image ray has to be intersected with the known water surface (see Fig. 6). Thanks to the lev-
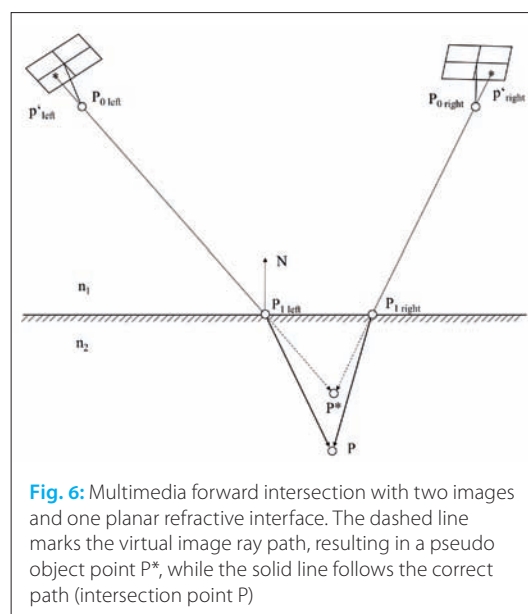

Fig. 6: Multimedia forward intersection with two images and one planar refractive interface. The dashed line marks the virtual image ray path, resulting in a pseudo object point P*, while the solid line follows the correct path (intersection point P)

. . .

Kenner, Robert; Marcia Phillips; Christian Hauck; Christin Hilbich; Christian Mulsow; Yves Buhler; Andreas Stoffel; Manfred Buchroithner (2017): New insights on permafrost genesis and conservation in talus slopes based on observations at Flüelapass, Eastern Switzerland; Geomorphology, Vol. 290, pp. 101–113, DOI: 10.1016/j.geomorph.2017.04.011

Kotowski, Rüdiger (1987): Zur Berücksichtigung lichtbrechender Flächen im Strahlenbündel; Schriftreihe der DGK, Reihe C, Vol. 330

Kröhnert, Melanie; Robert Meichsner (2017): Segmentation of environmental time lapse image sequences for the determination of shore lines captured by hand-held smartphone cameras; in: ISPRS Annals of the Photogrammetry, Remote Sensing and Spatial Information Sciences, Vol. IV-2/W4, pp. 1–8

Maas, Hans-Gerd (2015): On the Accuracy Potential in Underwater/Multimedia Photogrammetry; Sensors 2015, Vol. 15, No. 8, pp. 18140–18152, DOI: 10.3390/s150818140

Mulsow, Christian (2010): A flexible multimedia bundle approach; International Archives of Photogrammetry, Remote Sensing and Spatial Information Sciences, Vol. XXXVIII, Part 5, Commission V Symposium, Newcastle upon Tyne, UK

Mulsow, Christian, Hans-Gerd Maas (2014a): A universal approach for geometric modelling in underwater stereo image processing; Computer Vision for Analysis of Underwater Imagery (CVAUI), ICPR Workshop, Stockholm 2014

Mulsow, Christian; R Koschitzki; Hans-Gerd Maas (2014b): Photogrammetric monitoring of glacier margin lakes; Geomatics, Natural Hazards and Risk

Mulsow, Christian (2016): Ein universeller Ansatz zur Mehrmedien-Bündeltriangulation; in: Thomas Luhmann; Christian Schumacher (Hrsg.): Photogrammetrie – Laserscanning – Optische 3D-Messtechnik, Beiträge der Oldenburger 3D-Tage 2016, Verlag Herbert Wichmann

Rinner, Karl (1948): Problems of two-medium photogrammetry; Photogrammetric Engineering, Vol. 35, No. 2, pp. 275–282

Tewinkel, G. C. (1963): Water depths from aerial photographs; Photogrammetric Engineering, Vol. 29, pp. 1037–1042

elling behaviour of quiet water, the surface can be seen as planar, with surface normal in plumb-line direction. The refraction index for water can be extracted from empirical tables.

In the piercing point, the direction change of the refracted image ray can be computed after the following simple formula (Glassner 1989) which was derived from Snell's law:

$$L_2 = \frac{L_1}{n} + \left(\frac{C}{n} - \sqrt{1 + \frac{1}{n^2}(c^2 - 1)} \right) N_1$$

where

$$C = -N_1 \cdot L_1 \qquad\qquad n = \frac{n_2}{n_1}$$

in which:
L_1 : normalised incoming direction vector
L_2 : refracted direction vector (not normalised)
N_1 : surface normal vector of T_t in P_t
n : relative refractive index

So, for each corresponding image measurement an image ray can be reconstructed inside the water. In a final step, the corresponding image rays have to be intersected in order to determine the 3D coordinates of the underwater point. The accuracy can be estimated from the nearest distance of corresponding image vectors.

Another option for coordinate determination would be the inclusion of image measurements of point pairs into the bundle adjustment process. This would stabilise the triangulation, but means a significant increase of computing time due to multiple ray tracing for numerical linearisation inside the iterative adjustment. Therefore, as for conventional DTM extraction, the forward intersection procedure was applied.
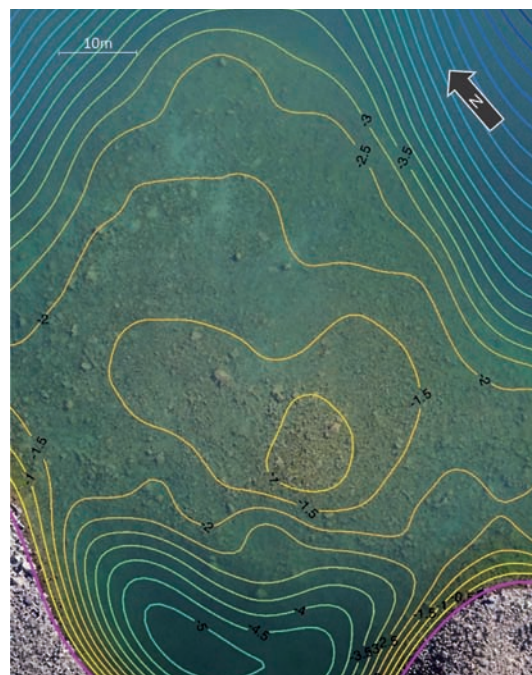
6   Results

The main goal of the project was the determination of an underwater DTM of the lobe area. Therefore, the analysis of results focuses on that. In order to quantify the refraction effects on the underwater point height data, two different DTM's were computed – one without and one with refraction compensation. As expected, the water depth was under-estimated when not taking the refraction into account (see Fig. 7 and Fig. 8). Fig. 9 illustrates the differences along a profile. The height offset is between 30-40%. The height accuracy was estimated from check-point data (see Table 1), resulting in a RMS to be 12cm (refraction considered). However, for the whole DEM the accuracy is heterogeneous, because of the varying imaging quality which mainly depends on water depth. As Figure 10 shows, structures in shallow water areas were imaged as sharp as onshore structures. However, with increasing water depth, the contrast as well as brightness drops drastically. Points could be successfully measured up to a water depth of ca. 3.5m when also accepting some low-quality image points.

For validation purposes, the DTM was intersected with the water level. The derived shore line was projected into the images in order to evaluate its fit. As one can see in Figure 7 and 8, the calculated shore line follows the real line very well.

7   Conclusion and outlook

The paper has shown a photogrammetric workflow for DEM generation from aerial images for regions that contain both land and underwater areas. An appropriate labelling of measured image points and a strict consideration of multimedia geometry in both image orientation and 3D point coordinate determination turned out to be crucial
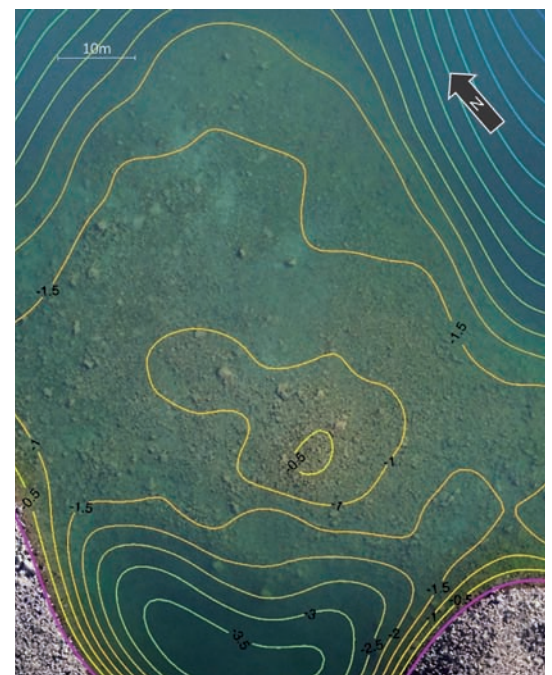

Fig. 7: DTM computed via multimedia forward intersection. The magenta line indicates the shoreline derived from intersection of DEM with water surface

Fig. 8: DTM computed via conventional forward intersection. Note the difference in depth range
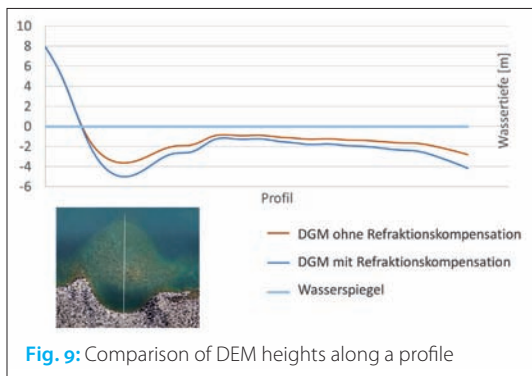
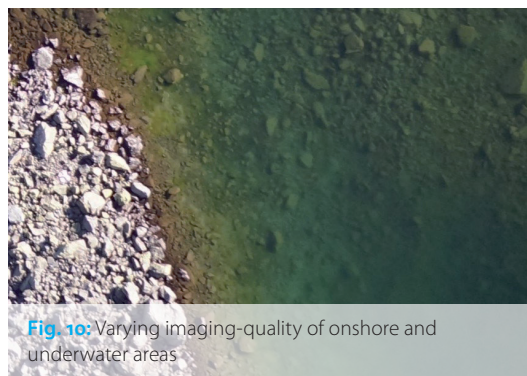**Fig. 9:** Comparison of DEM heights along a profile

Fig. 10: Varying imaging-quality of onshore and underwater areas

to achieve good accuracy for underwater points. When neglecting these effects, water depth is significantly underestimated.

A suitable strategy for aerial triangulation has been described. Images showing mainly onshore points should be triangulated first. The derived camera-parameters as well as orientation parameters should be fixed for a second run. In this step, images showing mainly underwater areas should be oriented. The proof-of-concept could be provided by processing the data with different parameter-settings. From comparative measurements of check-points, an RMS of 12cm for heights of underwater points could be estimated.

During the project, several ideas for improvement arose. First of all, the flight planning should be adjusted for the needs of multi-media photogrammetry. In order to improve the intersection-geometry, a camera with a larger opening-angle should be applied. Another option could be the use of oblique imagery. However, the camera axis should be tilted only slightly in order to keep the effects of water waves down to a certain level and to prevent total reflection. Furthermore, underwater control points should be installed in order to stabilize the orientation. The shore-line in the images might be extracted automatically by analysing the colour-changes (Kröhnert, et al.,2017), (Mulsow et al., 2014b). To refine the water-land transition of the generated DTM Initial values for the shore line can be derived by intersecting the DTM with the plane water-level, as already shown.